Title
Ash production and dispersal from sustained low-intensity Mono-Inyo eruptions

Journal
Bulletin of Volcanology, 78(8)

ISSN
0258-8900

Authors
Black, Benjamin A
Manga, Michael
Andrews, Benjamin

Publication Date
2016-08-01

DOI
10.1007/s00445-016-1053-0

Peer reviewed

Ash production and dispersal from sustained low-intensity Mono-Inyo eruptions

- Authors
- Authors and affiliations

- Benjamin A. Black
- Michael Manga
- Benjamin Andrews

Research Article
First Online: 02 August 2016

Abstract

Recent rhyolitic volcanism has demonstrated that prolonged low-intensity ash venting may accompany effusive dome formation. We examine the possibility and some consequences of episodes of extended, weak ash venting at the rhyolitic Mono-Inyo chain in Eastern California. We describe ash-filled cracks within one of the youngest domes, Panum Crater, which provide a textural record of ash venting during dome effusion. We use synchrotron-based X-ray computed tomography to characterize the particles in these tuffisites. Particle sizes in well-sorted tuffisite layers agree well with grain size distributions observed during weak ash venting at Soufrière Hills Volcano, Montserrat, and yield approximate upper and lower bounds on gas velocity and mass flux during the formation of those layers. We simulate ash

dispersal with Ash3d to assess the consequences of long-lived Mono-Inyo ash venting for ash deposition and the accompanying volcanic hazards. Our results highlight the sensitivity of large-scale outcomes of volcanic eruptions to small-scale processes.

Keywords

Mono-Inyo eruptions Rhyolitic volcanism Ash venting X-ray computed tomography Ash3d

Editorial responsibility: C. Bonadonna

Introduction

The Mono-Inyo craters are a sickle-shaped chain of rhyolitic domes and craters that extends to the northwest of the Long Valley Caldera in California (Sieh and Bursik 1986; Bursik and Sieh 1989; Hildreth 2004). Eruptions have occurred in the recent past, including eruptions along the Mono-Inyo chain ~700 years ago (Sieh and Bursik 1986) and at Paoha Island ~200 years ago (Bailey 1989), and the majority of eruptions have occurred within the past 20 ka. The total erupted volume of the Mono-Inyo craters is ~5.8–9.3 km^3 (Miller 1985; Sieh and Bursik 1986; Hildreth 2004). Their recent activity—combined with their location (~40 km east of Yosemite, CA, and ~370 km northwest of Las Vegas, NV), rhyolitic composition, and propensity for explosive eruptions (Sieh and Bursik 1986)—renders the Mono-Inyo craters one of the most potent volcanic hazards in CA, USA (Hill et al. 1997).

The Chaitén eruption of 2008–2009 and the Cordón Caulle eruption of 2011 in Chile presented the first opportunities to employ modern geological and geophysical tools to observe a rhyolitic effusive eruption in progress (Lara 2009; Watt et al. 2009; Alfano et al. 2011; Bernstein et al. 2013; Pallister et al. 2013; Tuffen et al. 2013; Castro et al. 2013; Castro et al. 2014; Schipper et al. 2013). One of the most surprising aspects of the Chaitén eruption was the sustained, low-intensity ash production that followed the initial Plinian phase (Lara 2009; Carn et al. 2009). After partial dome collapse on February 19, 2009, ash production and low-altitude injection continued until the end of the eruption in late 2009 and coincided with gradual dome growth (Lara 2009; Carn et al. 2009; Pallister et al. 2013). During the June 2011 eruption at Cordón Caulle, the initial climactic phase similarly transitioned to weeks of lower-intensity ash venting accompanied by a weak plume (Bonadonna et al. 2015a; Pistolesi et al. 2015). Ash-filled cracks (called tuffisite) are abundant within blocks and bombs at Chaitén and at Cordón Caulle and have been interpreted as evidence of shear fracturing and as pathways for degassing during dominantly effusive phases (Castro et al. 2012; Schipper et al. 2013; Castro et al. 2014; Saubin et al. 2016; Kendrick et al. 2016).

In this work, we document the distribution of tuffisite-filled cracks at Panum Crater that contain ash produced during the North Mono eruptions <700 years ago (Sieh and Bursik 1986). We characterize the tuffisite using thin sections and X-ray computed tomography (XRCT). We suggest that, like the tuffisites from Chaitén and Cordón Caulle, these features may record past low-intensity ash production during dome effusion in the Mono-Inyo region. Estimates of mass flux from grain size distribution are consistent with protracted, unsteady venting. We use Ash3d (Schwaiger et al. 2012; Mastin et al. 2013) to simulate the transport and deposition of ash from a small, sustained, rhyolitic Mono-Inyo eruption. The goal of these simulations is to assess the consequences of ash venting for the Long Valley region and to explore quali-tative differences between ash dispersal during sustained low-intensity venting versus more explosive eruptions. We show that for a given total eruption volume, as the eruption duration increases and column heights decrease, the ash dispersal process is increasingly sensitive to topography and also samples a larger range of wind directions (diminishing the spatial unpredictability of cumulative ashfall). The patterns of ash dispersal from sustained, weak ash venting are fundamentally different from dispersal from short-lived, vigorous eruption columns. These results agree with observations and modeling of weak, wind-affected plumes during eruptions at Mt. Etna, Cordón Caulle, and elsewhere (Scollo et al. 2007; Barsotti et al. 2010; Scollo et al. 2013; Bonadonna et al. 2015a; Bonadonna et al. 2015b; Pistolesi et al. 2015).

Geologic background

The Long Valley region is situated at the boundary between the Sierra Nevada and the Basin and Range Province (Fig. 1) and has hosted a rich history of magmatism. Beginning ~4.5 Ma, Basin and Range extension promoted decompression melting in the underlying mantle (Hildreth 2004). The ensuing magmatism included mafic and dacitic eruptions that ultimately gave way to the 2.2–1.4 Ma Glass Mountain rhyolites (Metz and Mahood 1985; Bailey 1989; Bailey 2004). The eruption of the 600 km^3 Bishop Tuff 767.1 ± 0.9 ka (Crowley et al. 2007) spanned only ~6 days (Wilson and Hildreth 1997) and formed the Long Valley Caldera. Following the eruption of the Bishop Tuff and the emplacement of the postcaldera Early Rhyolite (Bailey 2004), the pace of magmatism in the Long Valley region declined markedly (Hildreth 2004).

Open image in new window

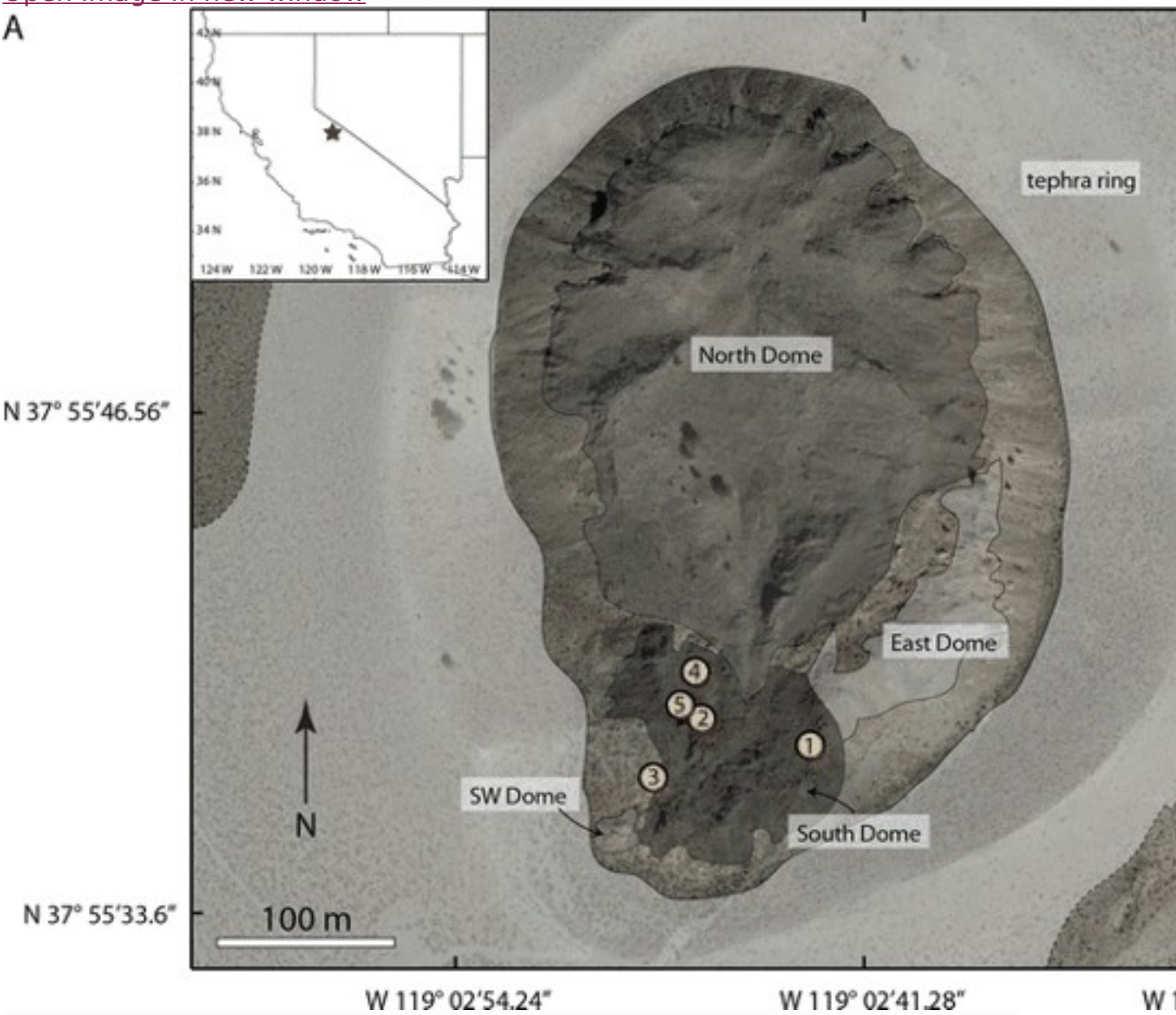

Fig. 1
a Map of Panum Crater, simplified from Sieh and Bursik (1986) and overlain on satellite imagery from Google Earth. The locations of tuffisite samples are labeled with *yellow circles* and annotated with *site numbers*. **b** Field photograph of site 1. **c** Field photograph of site 4. **d** Field photograph of site 5

Mono-Inyo volcanism initiated ~50 ka, and the most recent Mono-Inyo eruptions occurred in the fourteenth century (Miller 1985; Sieh and Bursik 1986). Even younger volcanism may have taken place in the past 200 years at Paoha Island in Mono Lake (Bailey 1989). Because the Mono-Inyo crater chain is outside the ring-fault zone of Long Valley Caldera, and

because eruption rates and seismic tomography suggest that the main Long Valley magma chamber may be moribund, Hildreth (2004) has argued that the Mono-Inyo craters originate from a separate magmatic system that largely does not tap the chamber that formed the Bishop Tuff. Thus, while a unified set of processes have likely encouraged mantle melting and basaltic intrusion beneath the Long Valley region, these basaltic melts have focused in several distinct loci, most recently beneath the Mono-Inyo chain (Hildreth 2004). Crustal melting probably feeds the dominantly rhyolitic Mono-Inyo eruptions, while range-front faulting controls the distribution of volcanism (Bursik and Sieh 1989).

During the period of activity in the fourteenth century, within a span of several years, a series of eruptions took place at both the northern and southern extremities of the Mono-Inyo chain (Miller 1985; Sieh and Bursik 1986). At the southern end of the chain, the Inyo dike triggered formation of multiple phreatic craters and rhyolitic vents (Miller 1985; Mastin and Pollard 1988; Mastin 1991; Nawotniak and Bursik 2010). At the northern end of the chain, an initial sub-Plinian phase gave way to pyroclastic flows and surges, followed by extrusive formation of lava flows and domes (with a total extrusive volume of ~0.44 km^3 dense rock equivalent; Sieh and Bursik 1986).

While several vents contributed to this activity, Panum Crater has been described in particular detail. Panum Crater (Fig. 1) is situated near the southern edge of Mono Lake; the crater is surrounded by a tephra ring (with angular ash, lapilli, and rare small blocks), and within the crater, there are several small rhyolitic plugs known as North Dome, South Dome, East Dome, and Southwest Dome (Sieh and Bursik 1986). The excavation of the crater postdates the North Mono Plinian ashfalls and was accompanied by a series of pyroclastic flows and surges and at least one block-and-ash flow (Sieh and Bursik 1986). Radiocarbon dates from charred wood fragments within Panum deposits yield a weighted average date of 1324–1365 A.D. (Sieh and Bursik 1986).

The thickest ashfall deposits from Mono-Inyo eruptions are often locally well preserved and have been described by Sieh and Bursik (1986), Nawotniak and Bursik (2010), and Bursik et al. (2014). As described by these authors, many past explosive episodes have produced Plinian or sub-Plinian columns that exceed the column heights of 1–7.7 km we consider here. The durations of these explosive events may be only hours to days (e.g., Nawotniak and Bursik 2010), and some deposits are highly elongated (e.g., Bursik et al. 2009). Short-lived plumes may have reached up to 20 km altitude (Nawotniak and Bursik 2010). The premise of the present work is that in addition to these explosive episodes, low-intensity ash production (which is difficult to detect from distal deposits but may be recorded by tuffisite veins)

may have accompanied some Mono-Inyo eruptions. Despite their limited volume, such episodes may have different consequences as a result of their potential for month-long activity (Barsotti et al. 2010).

Distribution of ash-filled cracks at Panum Crater

As viscous silicic magmas ascend through conduits, high strain rates can produce shear fractures (e.g., Goto 1999; Tuffen et al. 2003; Gonnermann and Manga 2003; Neuberg et al. 2006). Given sufficient time, magma can efficiently degas through interconnected fracture networks (Castro et al. 2012). Consequently, at strain rates that are high enough to promote shear fracturing and low enough to permit degassing on the time scale of ascent, shear fractures have been hypothesized to facilitate a transition to effusive degassing (Gonnermann and Manga 2003). However, shear fragmentation combined with gas release through fractures also causes ash venting in tandem with effusive eruption (Kendrick et al. 2016). This process is preserved geologically in the form of tuffisite-filled veins (Castro et al. 2012).

Here, we document the distribution and properties of tuffisites at the South Dome of Panum Crater in the Mono-Inyo chain (Fig. 1). The South Dome has been interpreted as one of the final plugs of material erupted from the Panum conduit (Sieh and Bursik 1986). Because the dome is modest in scale, effusive flow has not erased tuffisites and other textural features, and the well-exposed South Dome therefore offers a privileged snapshot of the uppermost conduit (Befus et al. 2015). We have not observed tuffisite veins at Panum's North Dome, which may either indicate that the tuffisites were destroyed during extrusion or that shear fracturing and ash venting did not accompany the extrusion of North Dome.

The South Dome tuffisites range from well-sorted, fine-grained sintered ash to poorly sorted blocks—often within the same vein (Fig. 1c). Clasts are predominantly juvenile glass, but lithics include granitoid and mafic fragments (Fig. 2b). Layering, grain size sorting, and truncation surfaces can collectively form a complex internal stratigraphy within individual tuffisites (Fig. 2c, d, g, h). The tuffisite veins are often embedded in coarsely vesicular pumice clasts. At the contact surfaces, the pumice grades into a millimeter-thick gray glassy rind (Fig. 2f).

Open image in new window

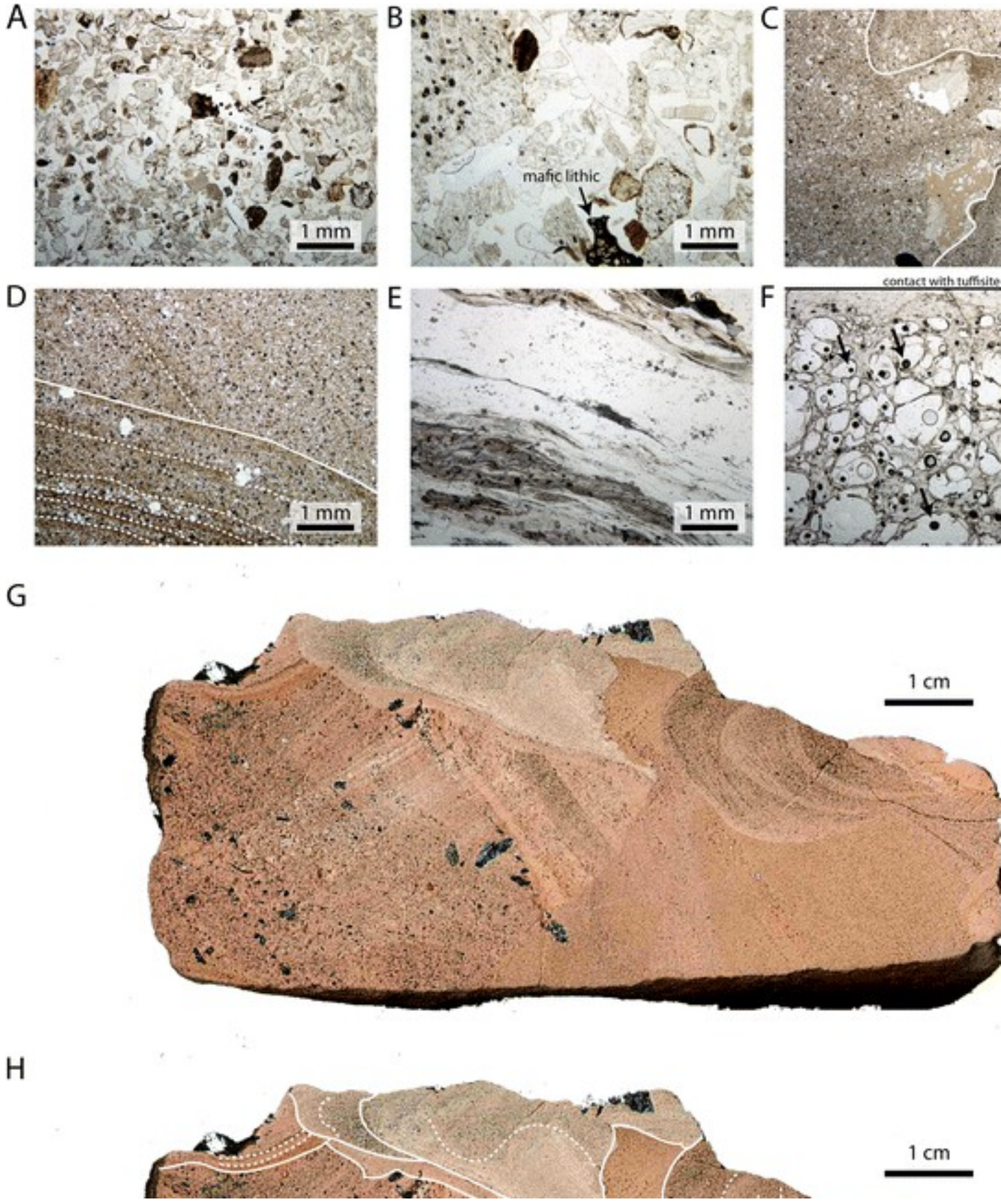
A
1 mm
B
mafic lithic
1 mm
C
D
1 mm
E
1 mm
F
contact with tuffisite
G
1 cm
H
1 cm

Fig. 2
Panum Crater samples in thin section and hand sample. **a** Fine, well-sorted tuffisite from site 1 at Panum Crater. **b** Coarse tuffisite with rare mafic lithics, also from site 1 at Panum Crater. **c** Very fine tuffisite from site 5 at Panum Crater. **d** Very fine tuffisite from site 5 at Panum Crater. Truncation surface records at least two generations of ash transport. **e** Obsidian from South Dome. **f** *Gray glass* from South Dome with bubbles (examples indicated by *black arrows*); the fine-grained upper margin was in contact with a small tuffisite vein. Some *light-colored circular shapes* may be imperfections in the epoxy. **g** Saw-cut slab from site 5 at Panum Crater displaying the complex stratigraphy of cross-cutting and truncated layering with variable grain size and sorting. **h** Saw-cut slab from G with truncation surfaces denoted with *solid white lines* and internal layering denoted with *dashed lines*

These observations place some qualitative constraints on the temporal duration of individual ash venting pulses, which in turn help to characterize the overall history of hybrid lava extrusion and ash venting at Panum. Sintering of the ash particles within fractures gradually decreases permeability and can eventually choke off degassing pathways (Kendrick et al. 2016; Saubin et al. 2016). While many Panum tuffisites are sintered, the low degree of sintering in a few Panum tuffisites may indicate that at the time the eruption terminated, these cracks were still viable passages for degassing and ash venting. We postulate that the complex layering and stratigraphy within the Panum tuffisites (Fig. 2g) may reflect pathways that have repeatedly clogged and reactivated, perhaps due to cycles of particle accumulation and sintering and further shear stress-induced fracturing (Gonnermann and Manga 2003; Tuffen et al. 2003; Saubin et al. 2016). Thus, both the stratigraphy within the tuffisites and the vesiculation in the host rhyolite support prolonged activity including multiple episodes of ash venting during the Panum eruption. However, beyond this qualitative conclusion, we are currently unable to bracket the duration of past ash release events.

X-ray tomography

Because the particles in the tuffisites are sintered, we cannot measure particle size using laser diffraction or sieve analyses. Instead, we characterized particle size and shape for three tuffisite samples from Panum dome using XRCT. We collected XRCT data on beamline 8.3.2 at the Lawrence Berkeley National Laboratory Advanced Light Source. Imaging was performed with monochromatic 22-keV X-rays, 1024 projections, and an imaging volume of 2560 × 2560 × 1788 cubic voxels, with a voxel side length of 1.27 μm. Reconstructions were performed with Octopus software. The three samples were collected at site 5 on the South Dome and include two well-sorted extremely fine tuffisites and one medium tuffisite specimen (samples 5A, 5B, and 5C as shown in Fig. 3a–c, respectively).

Open image in new window

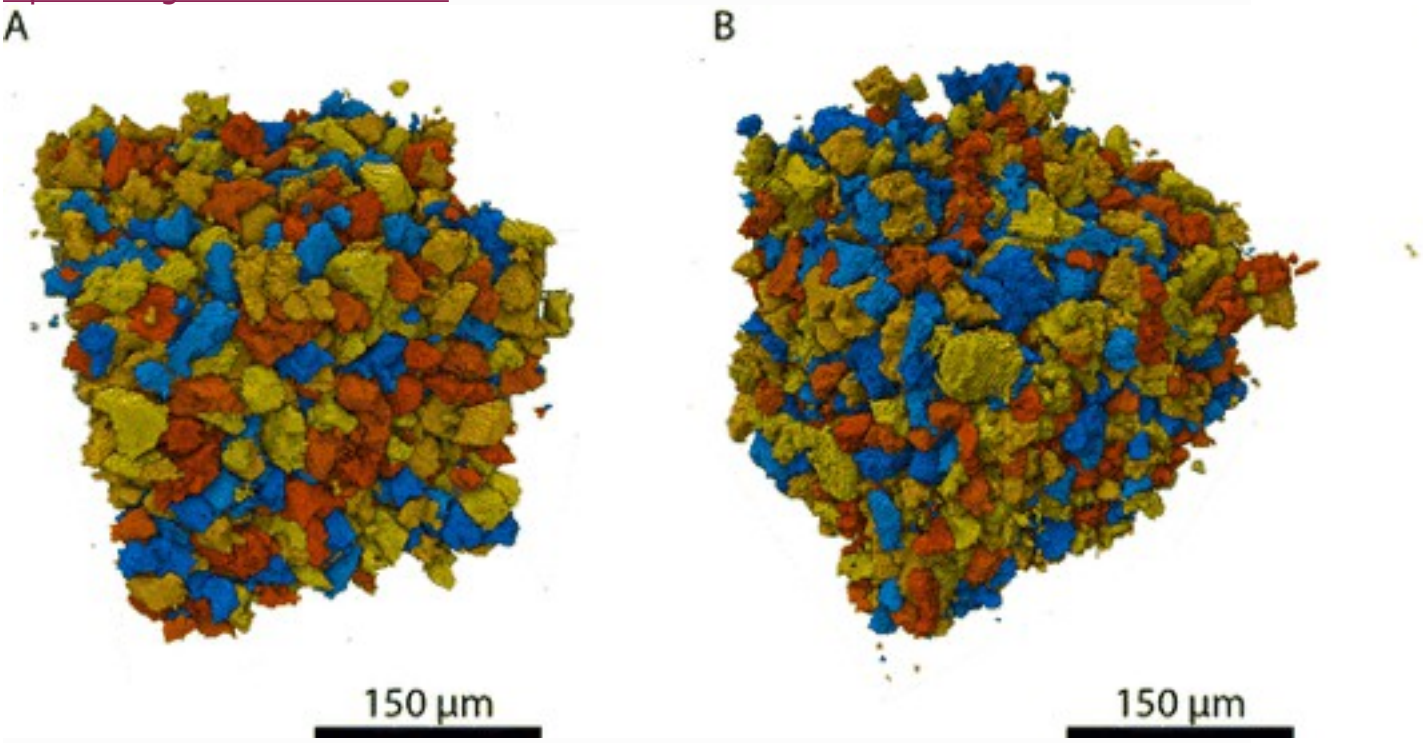

Fig. 3
X-ray computed tomography of three tuffisite samples from site 5 at Panum Crater. Clasts have been artificially colored to illustrate the results of the automated segmentation to identify individual grains. **a** Fine-grained, well-sorted tuffisite sample 5A. **b** Fine-grained, well-sorted tuffisite sample 5B. **c** Medium-grained tuffisite sample 5C

The XRCT analyses provide three-dimensional information about the structure, shape, and size distribution of the ash particles and pores within the tuffisite samples (Fig. 3). We processed the reconstructed data with Avizo® Fire 8.1. We used the interactive thresholding, separate objects, labeling, and volume fraction modules in Avizo® (in that order) to quantitatively analyze the pore space and ash population.

The porosity in the tuffisites ranges from 0.50 to 0.66. The grain size ranges from several microns to block-sized fragments (observed in outcrop—see Fig. 1—but not represented in the samples we analyzed via XRCT). The largest grain diameters measured via XRCT reached ~0.2 mm. In Tables 1 and 2, we summarize grain size data from XRCT analyses of samples from site 5 at Panum Crater. We emphasize that the textures in tuffisites at Panum are highly diverse and that we therefore do not expect the three samples we analyzed via XRCT to capture the total grain size distribution within the tuffisites.

Table 1

Grain size properties from Panum tuffisites measured via XRCT and from Bonadonna et al. (2015a) for Cordón Caulle ashfall (their Table 1; Voronoi tessellation method) and Alfano et al. (2016) for the total grain size distribution of Chaitén ashfall

Sample	5 %	16 %	50 % Md_ϕ	84 %	95 %	σ_ϕ
Panum 5A	6.65	6.34	6.04	5.78	5.62	0.26
Panum 5B	6.63	6.33	5.94	5.62	5.44	0.32
Panum 5C	5.08	4.45	3.92	3.57	3.34	0.35
Cordón Caulle		0.5	−1.9	−4.3		2.4
Chaitén		5.1	2.7	0.3		2.4

Reported as mass percentile in ϕ units,
where $\square = -\log_2(\square_{1\ mm})\phi = -\log_2(d_{1\ mm})$

Table 2
Aggregation-adjusted grain size distribution used in Ash3d simulations

ϕ	1	2	2.1	2.2	2.3	2.4	2.5	3
Grain size (mm)	0.5	0.25	0.23	0.22	0.2	0.19	0.18	0.125
Mass fraction	0.026	0.05	0.087	0.175	0.35	0.175	0.087	0.049
Shape factor	0.44	0.44	1	1	1	1	1	0.44
Density (kg/m^3)	1000	1200	1200	1200	1200	1200	1200	1800

Following the procedure described by Mastin et al. (2016), the total grain size distribution from the June 24, 2005 ash venting at Soufrière Hills Volcano, Montserrat (Cole et al. 2014), has been adjusted to account for aggregation of the finest particles (partial aggregation for $4 > \phi > 2$, 100 % aggregation for $\phi > 4$). We assume that the mean grain size of the aggregates is $\phi = 2.3 \pm 0.1$ (Mastin et al. 2016) and that their shapes can be approximated as spheres

As shown in Table 2, the Panum tuffisites we analyzed are finer and better sorted (with $\sigma_\phi = 0.26–0.35$ in phi units) than fall deposits from the Chaitén and Cordón Caulle eruptions (Watt et al. 2009; Bonadonna et al. 2015a; Alfano et al. 2016) and the sub-Plinian deposits at Panum that preceded dome extrusion (Heiken and Wohletz 1987). However, the grain size of these Panum tuffisites is remarkably similar (Fig. 4) to the modal grain size of ashfall from weak, precursory ash venting at Soufrière Hills Volcano, Montserrat (Cole et al. 2014). Individual tuffisite patches are better sorted

than the ashfall, but taken together, the three tuffisite samples for which we obtained XRCT data span the peak in the Soufrière Hills grain size distribution (Fig. 4). The similar grain size of Panum tuffisites and Soufrière Hills ashfall in conjunction with well-sorted individual tuffisite patches suggests that the grain size distribution observed in ashfall during weak venting may result from a mixture of ash vented from multiple, simultaneously active cracks, each with a distinctive grain size. This interpretation is consistent with observations of the vent area during ash venting at Soufrière Hills Volcano (Cole et al. 2014).

Open image in new window

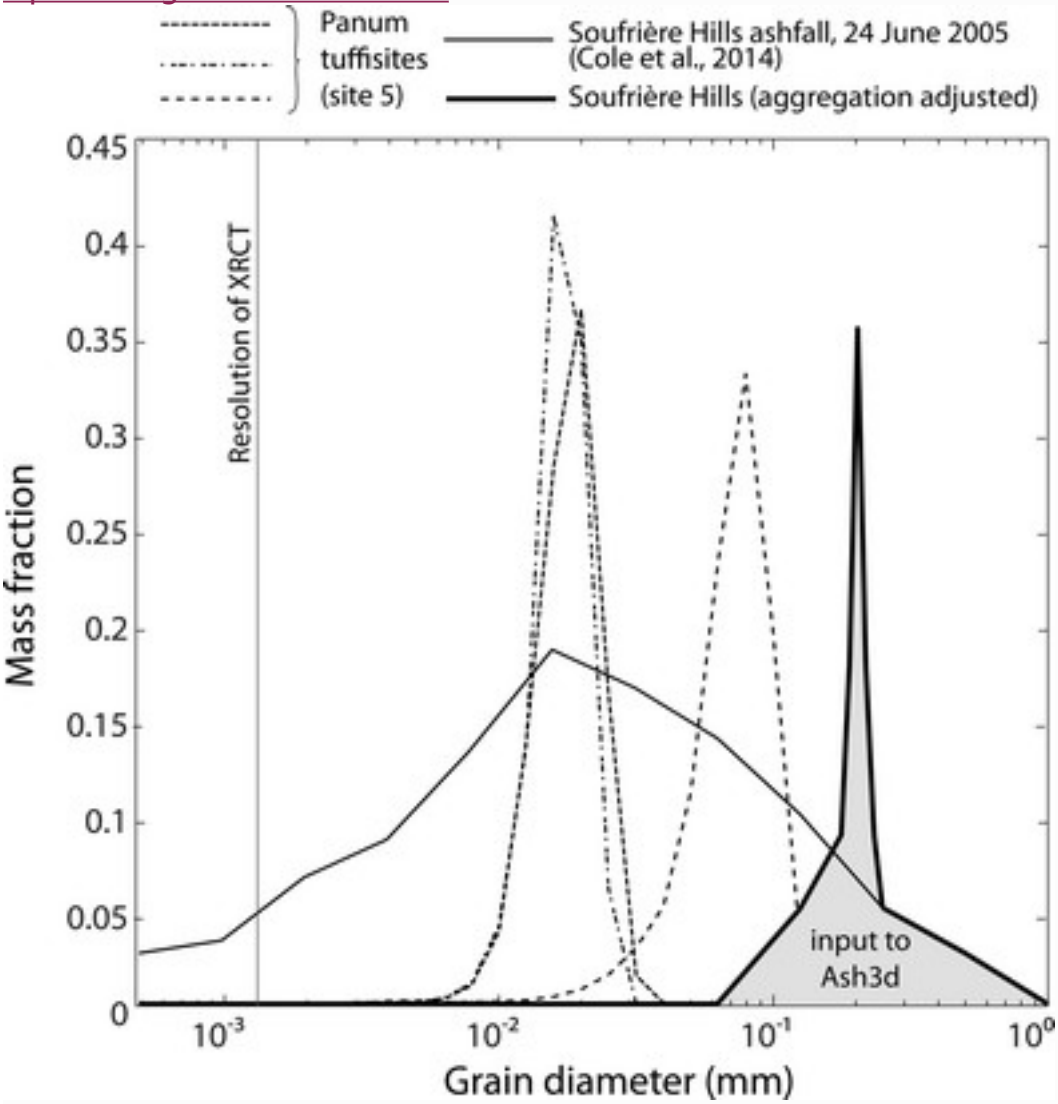

Fig. 4
Grain size distributions from Panum Crater tuffisites (from X-ray computed tomography data), from the June 24, 2005 ash venting at Soufrière Hills Volcano, Montserrat (Cole et al. 2014), and after adjusting the June 24, 2005 Soufrière Hills ashfall to account for aggregation (Mastin et al. 2016)

Constraints on gas velocities in cracks

The well-sorted grain size distributions within individual layers record flow conditions during their emplacement. In this section, we develop the implications of the XRCT-derived grain size distributions shown in Fig. 4 for the gas velocities during flow, and consequently, for the mass flux at the time, these ash particles were in transit through cracks in the Panum dome. We acknowledge the following three important caveats: the complex stratigraphy within individual tuffisite-filled cracks suggests that flow within the cracks was not steady, grain size can vary widely from layer to layer, and the total crack area active at any given time is uncertain.

Fluidization refers to the development of fluid-like behavior when gas transiting through a bed of particles begins to suspend particles (Geldart 1973). When gas velocities are too low, particles act as a static, porous medium, and no fluidization occurs (Fueyo and Dopazo 1995). The minimum fluidization velocity (u_{mf}) is the minimum gas velocity required for drag to overcome the weight of the bed, initiating fluidization (Fueyo and Dopazo 1995).

$$□□□=9.4\times10-4[□□□]0.934□□1.8□0.87□gas0.066umf=9.4\times10-4[\Delta\rho g]0.934 Dp1.8\mu0.87\rho gas0.066 \quad (1)$$

where $\Delta\rho$ is the difference between the particle and gas density (ρ_{gas}), μ is the gas viscosity (taken here to be 2×10^{-5} Pa s), D_p is the particle diameter, and g is the gravitational acceleration, all in SI units. Equation (1) is valid only for $D_p < 0.1$ mm (Fueyo and Dopazo 1995). The void fraction at fluidization (ε_{mf}) can also be obtained from the following empirical expression (Wen and Yu 1966):

$$□□□=(114□□)1/3\varepsilon mf=(114\phi s)1/3 \quad (2)$$

where ϕ_s is a shape factor relating the surface area of a sphere to the actual surface area of a particle. Here, we assume that $\phi_s = 0.44$, which was the average shape factor measured among natural pyroclasts (Wilson and Huang 1979), although the shape factor defined by Wilson and Huang (1979) differs slightly from that of Wen and Yu (1966). The movement of material through cracks at Panum dome may have differed in important respects from an idealized bed of unconsolidated particles with vertical gas flow. In particular, the gas may have originated both through decompression and exsolution at depth due to the pressure gradient between the magma and the crack and also through diffusive degassing from the particles themselves (e.g., Saubin et al. 2016). Nevertheless, because we expect the vertical dimension of the cracks to be large relative to their lateral extent, most of the gas in which tuffisite particles were suspended probably originated from deeper in the fracture network, and the minimum fluidization velocity should give a reasonable lower bound on gas velocity during flow.

Conversely, the terminal velocity gives the threshold in excess of which larger particles would also have been entrained in the flow. In Fig. 5, we therefore plot the calculated terminal velocity as an upper bound on gas velocity, although if in reality some tuffisite particles were entrained and then fell back into the cracks, these calculations would represent an underestimate of the upper bound on exit velocity. The appropriate formulation for terminal velocity depends on the particle Reynolds number (Fueyo and Dopazo 1995).

$$\square\square\square=\square\square\square\square\square^{1.8}18\square\square\square\mathrm{Re}_{\mathrm{p}}<0.4 u_{ts}=\frac{g\Delta\rho D_p^{1.8}}{18\mu} \quad \text{for } \mathrm{Re}_p<0.4 \tag{3}$$

$$\square\square\square=\square\square[4(\square\square\square)^2225\square\square_{\mathrm{gas}}]^{1/3}\square\square\square0.4<\mathrm{Re}_{\mathrm{p}}<500 u_{ts}=D_p[4(g\Delta\rho)^2225\mu\rho_{gas}]^{1/3} \quad \text{for } 0.4<\mathrm{Re}_p<500 \tag{4}$$

where the particle Reynolds number $\mathrm{Re}_p = \rho_{gas} u D_p/\mu$.

Open image in new window

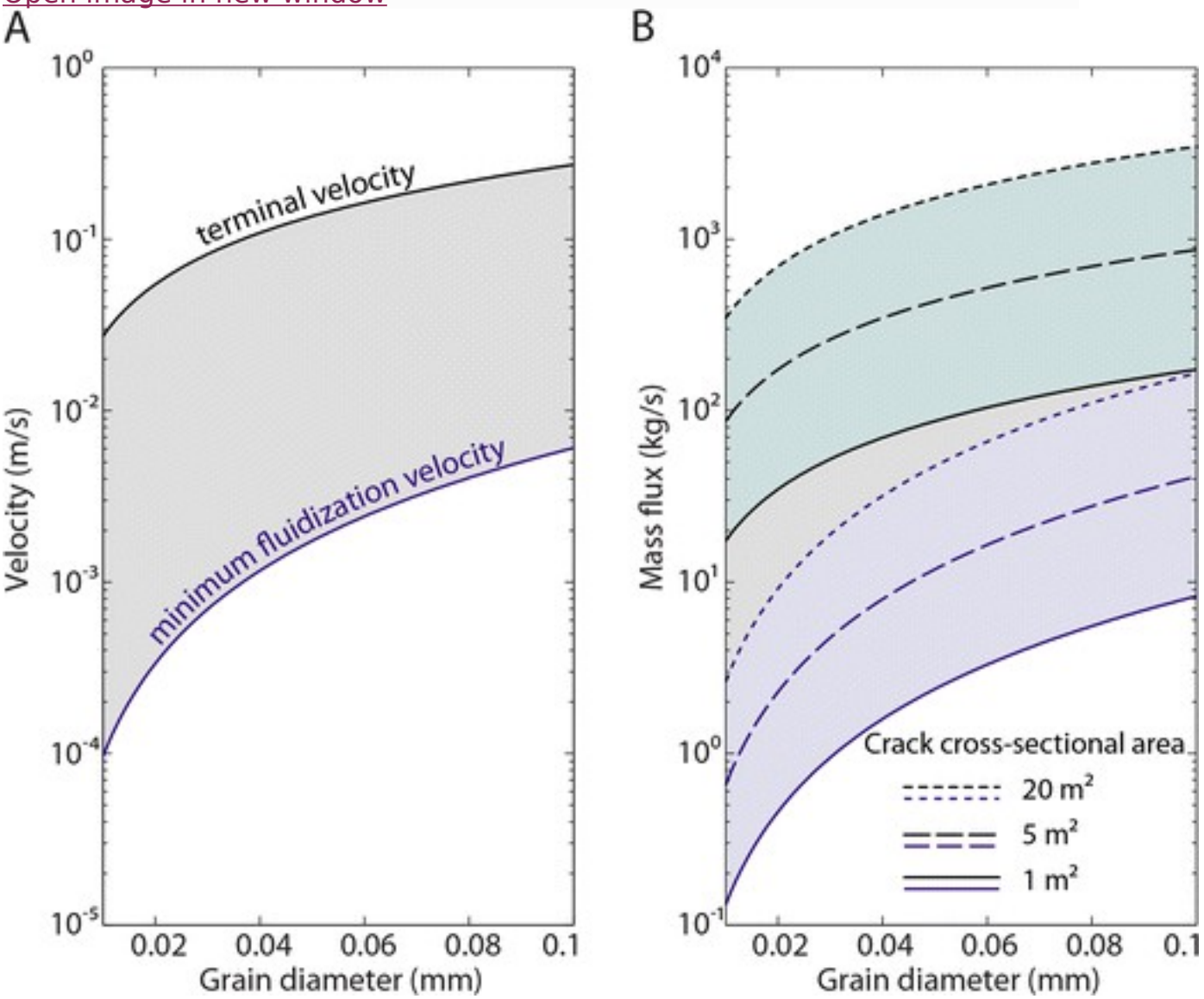

Fig. 5
Constraints on gas velocity and mass flux from grain sizes in tuffisites. **a** Minimum fluidization velocity provides a lower limit on the velocity during venting; the terminal velocity provides an upper limit (assuming negligible fallback). **b** Assuming an approximate crack cross-sectional area of 1, 5, or 20 m^2 (20 m^2 is an upper limit estimated from field exposures at Panum) in conjunction with a concentration given by the void space at fluidization (Wen and Yu 1966), the bounds on velocity yield upper and lower bounds on mass flux during venting

On the basis of the grain sizes in the tuffisites we analyzed with XRCT, we predict gas velocities of $10^{-4} - 10^{0}$ m/s (Fig. 5a). These lower and upper bounds on gas velocity, combined with the concentration at fluidization (Wen and Yu 1966) and an estimated crack cross-sectional area of 20 m^2, and neglecting the mass of the gas, imply relatively low mass fluxes of $10^{-1} - 10^{4}$ kg/s during venting (Fig. 5b). Coarse tuffisite veins (e.g., Fig. 1c) suggest that the mass flux during venting may occasionally have significantly exceeded 10^{4} kg/s.

Recent Mono-Inyo ashfall deposits have ranged in volume from ~0.01 to 0.1 km^3 dense rock equivalent (DRE), and the smaller eruptions are more common (e.g., Sieh and Bursik 1986; Nawotniak and Bursik 2010). The Panum block-and-ash-flow deposit has a volume of ~0.013 km^3 DRE, the volume of the Panum tephra ring is ~0.001 km^3 DRE, and the volume of Panum dome itself is ~0.012 km^3 DRE (Sieh and Bursik 1986). At Soufrière Hills Volcano, Cole et al. (2014) estimated bulk volumes of $1.7 \times 10^{-5} - 5.4 \times 10^{-5}$ km^3, equivalent to $7 \times 10^{-6} - 2 \times 10^{-5}$ km^3 DRE assuming ash deposit density of 1000 kg/m^3 and dense andesite density of 2600 kg/m^3 (Druitt et al. 2002), for individual episodes of syn-extrusive ashfall. We therefore consider scenarios in which either 0.001 or 0.02 km^3 DRE is vented during a hypothetical Mono-Inyo eruption; the latter value probably represents an upper limit on the volume that might be emitted during low-intensity activity.

Eruption of 0.001 km^3 DRE at ~10^{2} kg/s would require ~1 year. The tuffisite grain sizes observed via XRCT are thus consistent with protracted time scales for weak, unsteady ash venting.

The Ash3d model

We used Ash3d, a finite-volume Eulerian model, described more fully in Schwaiger et al. (2012) and Mastin et al. (2013), to investigate the implications of eruption duration for ash dispersal from small-volume Mono-Inyo eruptions. A fully probabilistic approach to simulating future eruption scenarios can encompass a wide range of possible parameters including column height, wind fields, and grain size distribution (e.g., Bonadonna et al. 2002; Cioni et al. 2003; Bonadonna 2006; Scollo et al. 2013; Biass et

al. 2014). Here, we consider a more limited parameter space (summarized in Table 3) to explore the consequences of eruption duration for the patterns of ash deposition and maximum airborne ash concentration.

Table 3

Eruption source parameters for Ash3d simulations

Volume (km^3 DRE)	Duration (days)	Plume height (km)	Plume height asl (km)
0.02	1	7.7	9.9
0.02	30	3.3	5.5
0.02	180	2.1	4.3
0.001	1	3.7	5.8
0.001	30	1.6	3.7
0.001	180	1.0	3.1

For grain size distribution, see Table 2. Start date for all simulations was January 1, 2000

The Ash3d model considers the advection, turbulent diffusion, and gravitational settling of a time-dependent injection of ash. Dispersal is sensitive to the initial distribution of mass, the grain size distribution, the wind fields, and the topography. In Ash3d, deposition occurs where horizontal advection of ash intersects with topography, resulting in artificially enhanced deposition along the upwind side of mountains and escarpments.

Comparison of Ash3d simulations with the dispersal of ash from event 5 of the 2009 eruption of Redoubt volcano in Alaska has shown that Ash3d can robustly reproduce key aspects of real events (Mastin et al. 2013). However, model results were sensitive to plume height, and the model slightly underpredicted deposit mass very close to and very far from the vent under these conditions (Mastin et al. 2013).

In our simulations, we assumed a grain size distribution based on the total grain size distribution from the June 24, 2005 ash venting at Soufrière Hills Volcano, Montserrat (Cole et al. 2014). We selected the June 24, 2005 pre-cursory ashfall because tephra produced during syn-extrusive venting at Soufrière Hills Volcano may have mixed with tephra from pyroclastic density currents (Cole et al. 2014). Prior work has demonstrated that aggregation of fine particles can strongly affect the patterns of ash distribution (Carey and Sigurdsson 1982; Cornell et al. 1983; Brazier et al. 1983; Rose and

Durant 2011; Brown et al. 2012). We therefore adjusted the size distribution to account for aggregation of the finest particles. Following Mastin et al. (2016), we assumed that for $\phi > 4$, all particles aggregated; that for $\phi < 2$, no particles aggregated; and that for $2 < \phi < 4$, the mass fraction aggregated increased linearly with ϕ from 0 to 1. We assume that the mean grain size of the aggregates is $\phi = 2.3 \pm 0.1$ (Fig. 4and Table 2) and that the aggregate shapes can be approximated as spheres (Mastin et al. 2016).

The model topography is the 1-arcmin resolution ETOPO1 dataset (Amante and Eakins 2009). We used year 2000 NOAA NCEP/NCAR Reanalysis wind fields with a 6-h temporal resolution (Kalnay et al. 1996). We do not aim to predict the specific patterns of ash dispersal and deposition from future eruptions, which will depend strongly on wind directions. Instead, because the wind fields and seasonality of future eruptions are unknown, we began all simulations on January 1. This January 1 start date in the simulations is arbitrary. Other start dates could lead to dispersal in other directions depending on prevailing winds but will not strongly affect our interpretations.

We summarize the eruption source parameters we considered in Table 3. As noted in the previous section, based on the volumes of previous eruptions at the Mono-Inyo craters, we consider eruption volumes of 0.001 or 0.02 km^3 DRE. During the Cordón Caulle eruption of 2011 and the Chaitén eruption of 2008–2009, weak syn-extrusive ash venting persisted for weeks to months. We therefore consider prolonged eruption durations of 30 and 180 days, and we compare the results of these simulations to simulations in which the same total volume is erupted in a single day. For an erupted volume of 0.001 km^3 DRE, this range of eruption durations implies a range of mass fluxes (10^2 to 10^4 kg/s) that is consistent with the upper and lower bounds on mass flux we estimated in "Constraints on gas velocities in cracks" section from Panum grain sizes. We use these mass fluxes to compute the volcanic plume height for each scenario in Table 3.

Volcanic plume height H depends on the flux of hot material and the stratification of the atmosphere and can be approximated as (Woods 2013)

$$H = \lambda B^{1/4} N^{-3/4} \quad (5)$$

where B is the effective buoyancy flux, N is the Brunt-Väisälä frequency (taken to be ~0.013 rad s^{-1}; Satheesan and Krishna Murthy 2002), and $\lambda \approx 5$ is an experimentally determined constant (Woods 2013). This expression applies to a calm, dry atmosphere. High wind speeds can reduce column height, whereas high relative humidity can increase column height (Degruyter and Bonadonna 2012). The buoyancy flux is a function of the heat flux and background temperature.

□=□□(□0−□□)□air□□B=Qg(T0−Ts)pairTs (6)

with mass flux Q, gravitational acceleration g, magma temperature T_0=1100 K, surface temperature T_s = 300 K, and air density ρ_{air} = 1.2 kg/m³. For a given total eruption volume, the mass flux is inversely proportional to the duration of the eruption. Column heights during prolonged, low-intensity eruptions may be correspondingly modest (Fig. 6).

Open image in new window

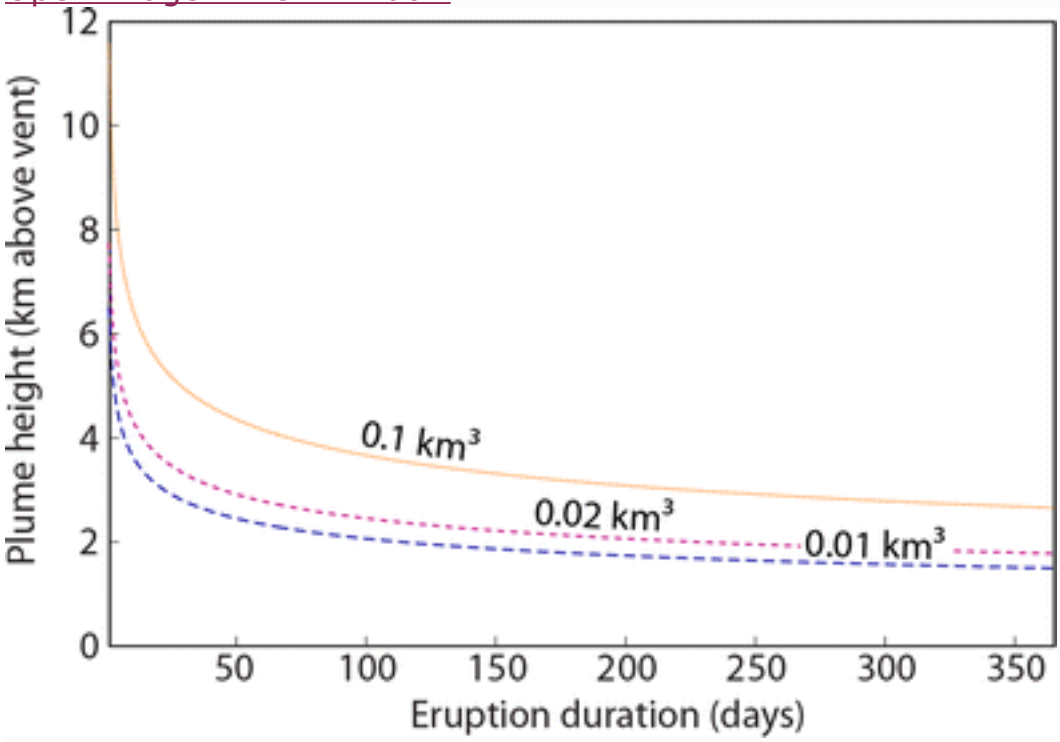

Fig. 6
Plume height for a range of total fallout volumes and eruption durations. Note that the elevation of Panum Crater is approximately 2100 m

Ash dispersal from sustained, low-level emissions from the Mono-Inyo chain

Our maps of ash dispersal and deposition (Figs. 7 and 8) should not be considered as predictions of the precise geography of ash deposition from a future Mono-Inyo eruption but rather as experiments in which we examine the effects of increasing eruption duration on the fate of ash. The Ash3d simulations illustrate several key features of sustained, low-intensity Mono-Inyo eruptions.

Open image in new window

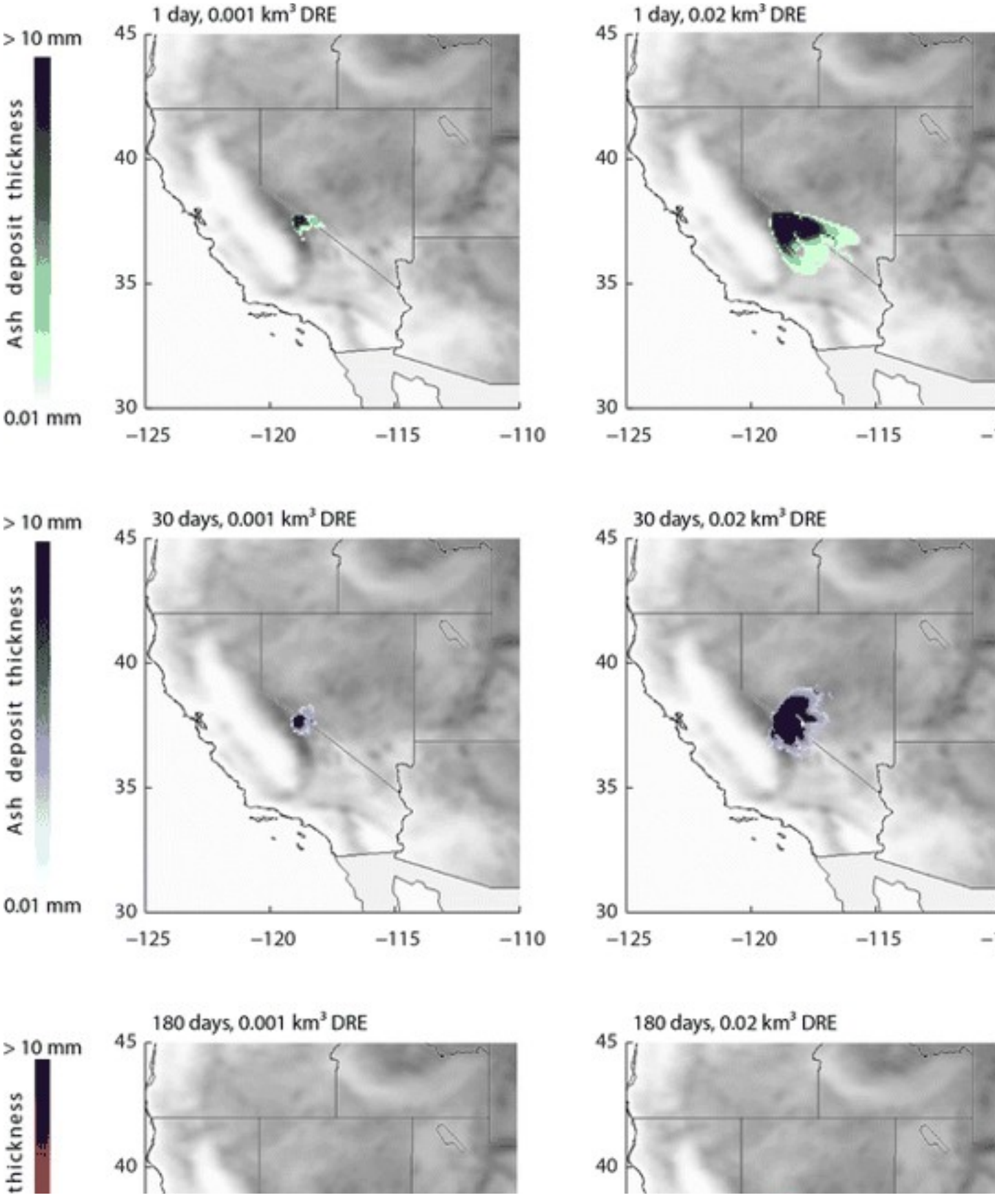
1 day, 0.001 km³ DRE
1 day, 0.02 km³ DRE
30 days, 0.001 km³ DRE
30 days, 0.02 km³ DRE
180 days, 0.001 km³ DRE
180 days, 0.02 km³ DRE
> 10 mm
Ash deposit thickness
0.01 mm
45
40
35
30
−125
−120
−115
−110

Fig. 7
Maps of ash deposit thickness from six hypothetical Mono-Inyo eruptions (*left and middle column*s) and rose diagrams showing wind directions (*right column*). The *gray scale* represents the topography of the southwestern USA (*white* is lowest, *dark* is highest)

Open image in new window

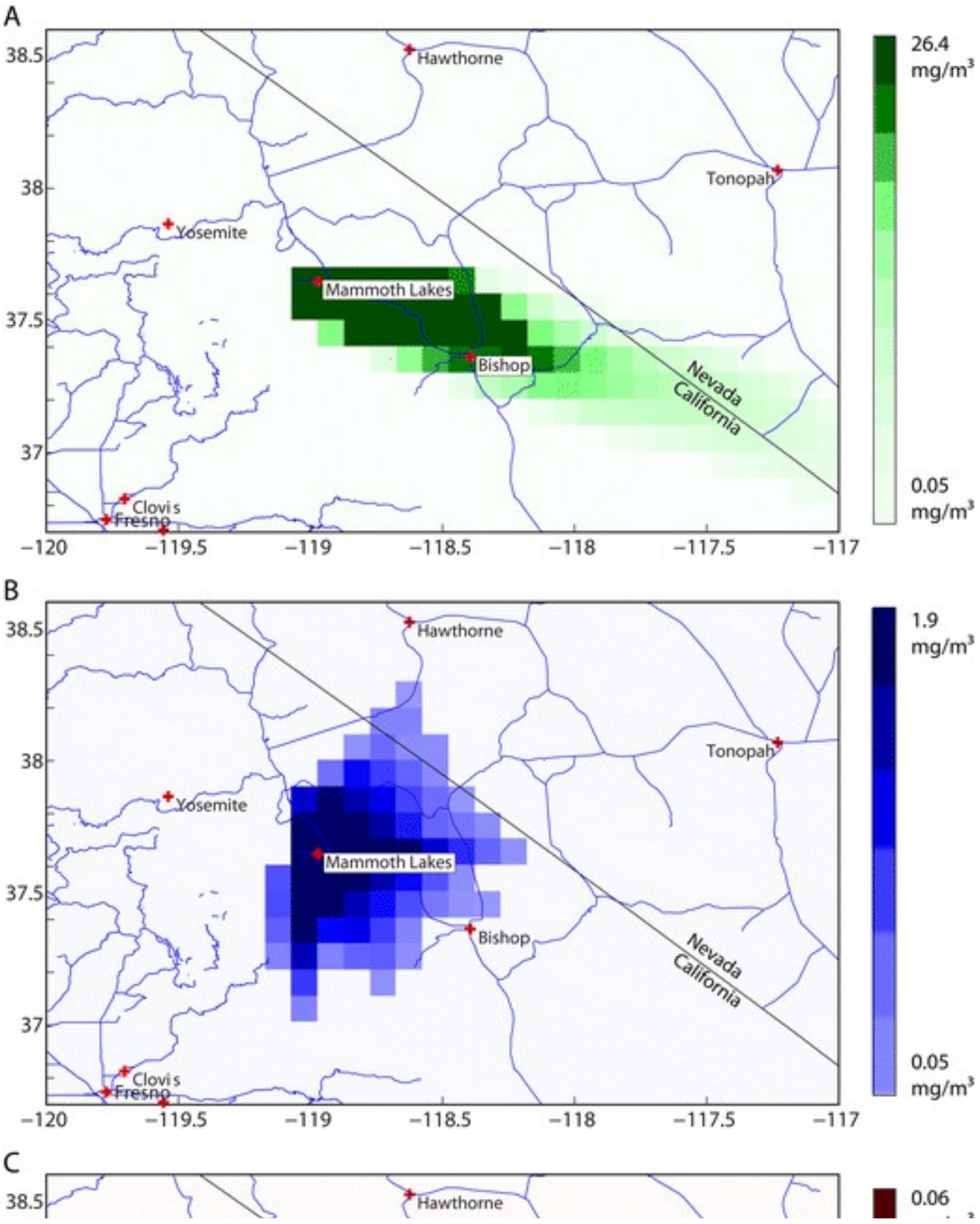
A
38.5
38
37.5
37
Hawthorne
Tonopah
Yosemite
Mammoth Lakes
Bishop
Nevada
California
Clovis
Fresno
−120
−119.5
−119
−118.5
−118
−117.5
−117
26.4
mg/m³
0.05
mg/m³
B
38.5
38
37.5
37
Hawthorne
Tonopah
Yosemite
Mammoth Lakes
Bishop
Nevada
California
Clovis
Fresno
−120
−119.5
−119
−118.5
−118
−117.5
−117
1.9
mg/m³
0.05
mg/m³
C
38.5
Hawthorne
0.06

Fig. 8
Maximum ash concentrations (at any altitude) during hypothetical 0.001 km^3 DRE Mono-Inyo eruptions. **a** Eruption spanning a single day. **b** Eruption spanning 30 days. **c**Eruption spanning 180 days. Note that the *color scale* differs in each case. The *blue lines*indicate roads

Ash dispersal from brief eruptions is sensitive to the wind directions that happen to prevail at the time of the eruption (e.g., Carey and Sparks 1986; Bursik et al. 2009; Burden et al. 2011; Mastin et al. 2013; Scollo et al. 2013); these wind directions will vary from day to day and season to season. In Fig. 7, we show that as duration increases, an eruption samples a larger range of these wind fields (Scollo et al. 2013). As a result, while the transport of ash on any given day will still be subject to chance, we expect the cumulative ashfall over the course of a prolonged eruption to be distributed more evenly around the vent (albeit in proportion to the long-term distribution of wind directions at the site). The maximum ash concentrations with increasing eruption duration (Fig. 8) show a similar pattern.

For a given total eruption size, longer eruptions correspond to lower mass fluxes and lower column heights. Ashfall and airborne particle concentrations from such eruptions are mostly confined within the Long Valley region (Figs. 7 and 8). These predictions are consistent with results from studies of prolonged eruptions at other volcanoes (e.g., Scollo et al. 2007; Scollo et al. 2013). For 0.001 km^3 DRE ash emitted over the course of 30–180 days, the maximum deposit thickness is 1–3 cm, and the deposit thickness is negligible in areas more than a few tens of kilometers from the vent. This result highlights the difficulty of detecting past episodes of low-intensity ash venting in the rock record. Sieh and Bursik (1986) noted that the East Dome at Panum has a thin, patchy tephra mantle. Given the scanty deposit thickness predicted by Ash3d after prolonged low-intensity venting, it would not be surprising if this scattered tephra and the tuffisite veins represent the only remnants of past syn-extrusive ash venting. This possibility underscores the importance of detailed examination of tuffisites to evaluate their use as a record of ash production during dominantly effusive eruptions (Kendrick et al. 2016; Saubin et al. 2016).

Consequences of a future low-intensity ash eruption in Eastern California

During the 2008 Chaitén eruption, several thousand people were evacuated, and the eruption severely impacted local agriculture and tourism (Lara 2009; Major and Lara 2013). Ash from the 2011 Cordón Caulle eruption led authorities to close the international airports at Buenos Aires on eight occasions (Raga et al. 2013). Light ashfall is not expected to collapse roofs or

cause direct human injuries, but even gentle ashfall can affect local travel and services (Hill et al. 1997), and fine volcanic ash can negatively impact respiratory health (Horwell and Baxter 2006; Barsotti et al. 2010).

In the context of our results and prior work, we consider the possible ramifications of future Mono-Inyo ash venting for residents of the Long Valley area and for air traffic. In a study of Mt. Etna, Italy, Barsotti et al. (2010) found that lower-intensity eruptions could actually increase the likelihood of critically elevated fine particle concentrations due to reduced dispersal in weak, low-altitude plumes. In our simulations, we assume that 100 % of the particles smaller than 125 μm, including the respirable (≤4 μm) and thoracic (≤10 μm) particles that pose the greatest health hazard (Barsotti et al. 2010), will aggregate. This assumption is motivated by studies of ash dispersal from sub-Plinian and Plinian eruptions (Cornell et al. 1983; Mastin et al. 2016). Thoracic material is present in the tuffisites (Fig. 4), suggesting that particles of this size could also comprise a substantial portion of the emitted ash prior to any aggregation. If significant fractions of the finest particles do not aggregate during protracted ash venting, such activity could pose a respiratory health hazard in the Mammoth Lakes region. Future work to evaluate the efficiency of aggregation during protracted ash venting is therefore warranted.

Many major airline routes pass directly over and near to the Mono-Inyo volcanoes. However, during protracted venting (ash emission spanning 30 or more days), the maximum predicted ash concentrations are confined to altitudes less than 6 km for the eruption parameters we consider (Table 3), whereas the maximum cruising altitude for commercial jets is more than 10 km. The highest ash concentrations also occur within ~50 km from the vent (Fig. 8). The Washington Volcanic Ash Advisory Center, in which the Mono-Inyo craters are located, does not employ defined threshold values for ash concentrations (http://www.ssd.noaa.gov/VAAC/program.html). The limited altitude and spatial extent of the ash during weak venting should mitigate the disruption to aviation, although unsteady venting and changing winds could cause conditions to vary significantly over the course of an eruption.

Although the likelihood of an eruption occurring in any given year is less than 1 %, the Mono-Inyo chain is the most probable source of a future eruption in the Long Valley region (Hill et al. 1997). Indeed, there is a conductive feature below Panum that has been interpreted as a partially molten magma column (Peacock et al. 2015) that could provide a source for future eruptions. A second conductive region beneath the slightly older South Coulee is less pronounced and has been interpreted as a cooled connection (Peacock et al. 2015). We suggest that assessments of volcanic

activity in the Mono-Inyo area should consider sustained, low-intensity ash venting as one possible aspect of future eruptions.

Conclusions

We consider the likelihood and implications of prolonged, low-intensity ash production from the Mono-Inyo craters in Eastern California. We use X-ray computed tomography to quantify the porosity and grain size distribution of tuffisites from Panum Crater. The well-sorted, 0.01–0.1-mm grains imaged via XRCT imply relatively low-mass fluxes of 10^{0}–10^{4} kg/s during the formation of specific tuffisite layers. The presence, grain size distribution, and complex internal stratigraphy of the tuffisites suggest that protracted ash venting occurred during the effusive phase of eruption at Panum Crater. We suggest that protracted ash venting may also occur during future effusive activity in the Mono-Inyo region. For a given eruption volume, as duration increases, both mass flux and buoyant column height decrease. Ash deposition is consequently more sensitive to surrounding topography, and ashfall tends to occur closer to the vent and to sample a larger range of wind directions. Simulations of protracted ash venting at Mt. Etna showed that low-intensity episodes can actually increase the likelihood of hazardous concentrations of particulate material, because particles remain in a smaller area close to the volcano (Barsotti et al. 2010). The implications of ash entombed in tuffisite veins at Panum Crater underscore the importance of small-scale processes for the style of volcanic eruptions and the dispersal of erupted material.

Notes

Acknowledgments

BAB and MM acknowledge support from National Science Foundation Hazards SEES grant EAR 1521855. The authors are indebted to Larry Mastin and Hans Schwaiger for their generous assistance with the Ash3d model and to the reviewers and the Associate Editor for their constructive comments. SNARL provided housing during field work. The XRCT analyses were conducted at the Advanced Light Source (ALS) at the Lawrence Berkeley National Laboratory. Beamline scientist Dula Parkinson provided essential advice and technical assistance.

References

1. Alfano F, Bonadonna C, Volentik AC, Connor CB, Watt SF, Pyle DM, Connor LJ (2011) Tephra stratigraphy and eruptive volume of the may, 2008, Chaitén eruption, Chile. Bull Volcanol 73:613–630CrossRefGoogle Scholar

2. Alfano F, Bonadonna C, Watt S, Connor C, Volentik A, Pyle DM (2016) Reconstruction of total grain size distribution of the climactic phase of a long-lasting eruption: the example of the 2008–2013 Chaitén eruption. Bull Volcanol 78:1–21CrossRefGoogle Scholar

3. Amante C & Eakins B W (2009) ETOPO1 1 arc-minute global relief model: procedures, data sources and analysis. US Department of Commerce, National Oceanic and Atmospheric Administration, National Environmental Satellite, Data, and Information Service, National Geophysical Data Center, Marine Geology and Geophysics DivisionGoogle Scholar

4. Bailey R A (2004) Eruptive history and chemical evolution of the precaldera and postcaldera basalt-dacite sequences, Long Valley, California: implications for magma sources, current seismic unrest, and future volcanism. US Department of the Interior, US Geological Survey, Number 1692Google Scholar

5. Bailey R A (1989) Geologic map of Long Valley caldera. Mono-Inyo craters volcanic chain, and vicinity, Eastern California: US Geological Survey Miscellaneous Investigations Series I-1933 1:11Google Scholar

6. Barsotti S, Andronico D, Neri A, Del Carlo P, Baxter P, Aspinall W, Hincks T (2010) Quantitative assessment of volcanic ash hazards for health and infrastructure at Mt. Etna (Italy) by numerical simulation. J Volcanol Geotherm Res 192:85–96CrossRefGoogle Scholar

7. Befus KS, Manga M, Gardner JE, Williams M (2015) Ascent and emplacement dynamics of obsidian lavas inferred from microlite textures. Bull Volcanol 77:1–17CrossRefGoogle Scholar

8. Bernstein M, Pavez A, Varley N, Whelley P, Calder E (2013) Rhyolite lava dome growth styles at Chaitén volcano, Chile (2008-2009): interpretation of thermal imagery. Andean Geol 40:295–309Google Scholar

9. Biass S, Scaini C, Bonadonna C, Folch A, Smith K, Höskuldsson A (2014) A multi-scale risk assessment for tephra fallout and airborne concentration from multiple Icelandic volcanoes—part 1: hazard assessment. Nat Hazards Earth Syst Sci 14:2265–2287CrossRefGoogle Scholar

10. Bonadonna C, Pistolesi M, Cioni R, Degruyter W, Elissondo M, Baumann V (2015b) Dynamics of wind-affected volcanic plumes: the example of the 2011 Cordón Caulle eruption, Chile. Journal of Geophysical Research: Solid Earth 120:2242–2261Google Scholar

11. Bonadonna C (2006) Probabilistic modelling of tephra dispersionGoogle Scholar

12. Bonadonna C, Cioni R, Pistolesi M, Elissondo M, Baumann V (2015a) Sedimentation of long-lasting wind-affected volcanic plumes: the example of the 2011 rhyolitic Cordón Caulle eruption, Chile. Bull Volcanol 77:1–19CrossRefGoogle Scholar

13. Bonadonna C, Macedonio G, Sparks R (2002) Numerical modelling of tephra fallout associated with dome collapses and Vulcanian explosions: application to hazard assessment on Montserrat. Geological Society, London, Memoirs 21:517–537CrossRefGoogle Scholar

14. Brazier S, Sparks R, Carey S, Sigurdsson H & Westgate J (1983) Bimodal grain size distribution and secondary thickening in air-fall ash layersGoogle Scholar

15. Brown R, Bonadonna C, Durant A (2012) A review of volcanic ash aggregation. Physics and Chemistry of the Earth, Parts A/B/C 45:65–78CrossRefGoogle Scholar

16. Burden R, Phillips J, Hincks T (2011) Estimating volcanic plume heights from depositional clast size. Journal of Geophysical Research: Solid Earth 116Google Scholar

17. Bursik M & Sieh K (1989) Range front faulting and volcanism in the Mono Basin, Eastern CaliforniaGoogle Scholar

18. Bursik M, Sieh K, Meltzner A (2014) Deposits of the most recent eruption in the southern Mono craters, California: description, interpretation and implications for regional marker tephras. J Volcanol Geotherm Res 275:114–131CrossRefGoogle Scholar

19. Bursik M, Kobs S, Burns A, Braitseva O, Bazanova L, Melekestsev I, Kurbatov A, Pieri D (2009) Volcanic plumes and wind: jet stream interaction examples and implications for air traffic. J Volcanol Geotherm Res 186:60–67CrossRefGoogle Scholar

20. Carey SN, Sigurdsson H (1982) Influence of particle aggregation on deposition of distal tephra from the May 18, 1980, eruption of Mount St. Helens volcano Journal of Geophysical Research: Solid Earth 87:7061–7072CrossRefGoogle Scholar

21. Carey S, Sparks R (1986) Quantitative models of the fallout and dispersal of tephra from volcanic eruption columns. Bull Volcanol 48:109–125CrossRefGoogle Scholar

22. Carn SA, Pallister JS, Lara L, Ewert JW, Watt S, Prata AJ, Thomas RJ, Villarosa G (2009) The unexpected awakening of Chaitén volcano, Chile. Eos, Transactions American Geophysical Union 90:205–206CrossRefGoogle Scholar

23. Castro JM, Bindeman IN, Tuffen H, Schipper CI (2014) Explosive origin of silicic lava: textural and δD–H_2O evidence for pyroclastic degassing during rhyolite effusion. Earth Planet Sci Lett 405:52–61CrossRefGoogle Scholar

24. Castro JM, Cordonnier B, Tuffen H, Tobin MJ, Puskar L, Martin MC, Bechtel HA (2012) The role of melt-fracture degassing in defusing explosive rhyolite eruptions at volcán Chaitén. Earth Planet Sci Lett 333:63–69CrossRefGoogle Scholar

25. Castro JM, Schipper CI, Mueller SP, Militzer A, Amigo A, Parejas CS, Jacob D (2013) Storage and eruption of near-liquidus rhyolite magma at Cordón Caulle, Chile. Bull Volcanol 75:1–17CrossRefGoogle Scholar

26. Cioni R, Longo A, Macedonio G, Santacroce R, Sbrana A, Sulpizio R & Andronico D (2003) Assessing pyroclastic fall hazard through field data and numerical simulations: example from Vesuvius. J Geophys Res Solid Earth 108Google Scholar

27. Cole P, Smith P, Komorowski J, Alfano F, Bonadonna C, Stinton A, Christopher T, Odbert H, Loughlin S (2014) Ash venting occurring both prior to and during lava extrusion at Soufriere Hills volcano, Montserrat, from 2005 to 2010. Geological Society, London, Memoirs 39:71–92CrossRefGoogle Scholar

28. Cornell W, Carey S, Sigurdsson H (1983a) Computer simulation of transport and deposition of the Campanian Y-5 ash. J Volcanol Geotherm Res 17:89–109CrossRefGoogle Scholar

29. Crowley J, Schoene B, Bowring S (2007) U-Pb dating of zircon in the bishop tuff at the millennial scale. Geology 35:1123–1126CrossRefGoogle Scholar

30. Degruyter W, Bonadonna C (2012) Improving on mass flow rate estimates of volcanic eruptions. Geophys Res Lett 39Google Scholar

31. Druitt T, Young S, Baptie B, Bonadonna C, Calder E, Clarke A, Cole P, Harford C, Herd R, Luckett R (2002) Episodes of cyclic Vulcanian explosive activity with fountain collapse at Soufrière Hills volcano, Montserrat. Memoirs-Geological Society of London 21:281–306CrossRefGoogle Scholar

32. Fueyo N & Dopazo C (1995) Fluidization fundamentals. In: Anonymous Pressurized Fluidized Bed Combustion. Springer 38–79Google Scholar

33. Geldart D (1973) Types of gas fluidization. Powder Technol 7:285–292CrossRefGoogle Scholar

34. Gonnermann HM, Manga M (2003) Explosive volcanism may not be an inevitable consequence of magma fragmentation. Nature 426:432–435CrossRefGoogle Scholar

35. Goto A (1999) A new model for volcanic earthquake at Unzen volcano: melt rupture model. Geophys Res Lett 26:2541–2544CrossRefGoogle Scholar

36. Heiken G, Wohletz K (1987) Tephra deposits associated with silicic domes and lava flows. Geol Soc Am Spec Pap 212:55–76Google Scholar

37. Hildreth W (2004) Volcanological perspectives on Long Valley, Mammoth Mountain, and Mono craters: several contiguous but discrete systems. J Volcanol Geotherm Res 136:169–198CrossRefGoogle Scholar

38. Hill DP, Bailey RA, Miller CD, Hendley JW II, Stauffer PH (1997) Future eruptions in California's Long Valley area—what's likely. US Geol Surv Fact Sheet:073–097Google Scholar

39. Horwell CJ, Baxter PJ (2006) The respiratory health hazards of volcanic ash: a review for volcanic risk mitigation. Bull Volcanol 69:1–24CrossRefGoogle Scholar

40. Kalnay E, Kanamitsu M, Kistler R, Collins W, Deaven D, Gandin L, Iredell M, Saha S, White G, Woollen J (1996) The NCEP/NCAR 40-year reanalysis project. Bull Am Meteorol Soc 77:437–471CrossRefGoogle Scholar

41. Kendrick JE, Lavallée Y, Varley N, Wadsworth FB, Lamb OD, Vasseur J (2016) Blowing off steam: tuffisite formation as a regulator for lava dome eruptions. Frontiers in Earth Science 4:41CrossRefGoogle Scholar

42. Lara LE (2009) The 2008 eruption of the Chaitén volcano, Chile: a preliminary report. Andean Geol 36:125–129Google Scholar

43. Major JJ, Lara LE (2013) Overview of Chaitén volcano, Chile, and its 2008-2009 eruption. Andean Geol 40:196–215Google Scholar

44. Mastin LG (1991) The roles of magma and groundwater in the phreatic eurptions at Inyo craters, Long Valley caldera, California. Bull Volcanol 53:579–596CrossRefGoogle Scholar

45. Mastin LG, Pollard D (1988) Surface deformation and shallow dike intrusion processes at Inyo craters, Long Valley, California. Journal of Geophysical Research: Solid Earth (1978–2012) 93:13221–13235CrossRefGoogle Scholar

46. Mastin LG, Schwaiger H, Schneider DJ, Wallace KL, Schaefer J, Denlinger RP (2013) Injection, transport, and deposition of tephra during event 5 at Redoubt volcano, 23 March, 2009. J Volcanol Geotherm Res 259:201–213CrossRefGoogle Scholar

47. Mastin LG, Van Eaton AR, Durant AJ (2016) Adjusting particle-size distributions to account for aggregation in tephra-deposit model forecasts. Atmospheric Chemistry and Physics Discussions 2016:1–48CrossRefGoogle Scholar

48. Metz JM, Mahood GA (1985) Precursors to the bishop tuff eruption: Glass Mountain, Long Valley, California. Journal of Geophysical Research: Solid Earth 90:11121–11126CrossRefGoogle Scholar

49. Miller CD (1985) Holocene eruptions at the Inyo volcanic chain, California: implications for possible eruptions in Long Valley caldera. Geology 13:14–17CrossRefGoogle Scholar

50. Nawotniak SK, Bursik M (2010) Subplinian fall deposits of Inyo craters, CA. J Volcanol Geotherm Res 198:433–446CrossRefGoogle Scholar

51. Neuberg JW, Tuffen H, Collier L, Green D, Powell T, Dingwell D (2006) The trigger mechanism of low-frequency earthquakes on Montserrat. J Volcanol Geotherm Res 153:37–50CrossRefGoogle Scholar

52. Pallister JS, Diefenbach A, Burton W, Muñoz J, Griswold J, Lara L, Lowenstern J, Valenzuela CE (2013) The Chaitén rhyolite lava dome: eruption sequence, lava dome volumes, rapid effusion rates and source of the rhyolite magma. Andean Geol 40:277–294Google Scholar

53. Peacock JR, Mangan MT, McPhee D, Ponce DA (2015) Imaging the magmatic system of Mono Basin, California, with magnetotellurics in three dimensions. Journal of Geophysical Research: Solid Earth 120:7273–7289Google Scholar

54. Pistolesi M, Cioni R, Bonadonna C, Elissondo M, Baumann V, Bertagnini A, Chiari L, Gonzales R, Rosi M, Francalanci L (2015) Complex dynamics of small-moderate volcanic events: the example of the 2011 rhyolitic Cordón Caulle eruption, Chile. Bull Volcanol 77:1–24CrossRefGoogle Scholar

55. Raga G, Baumgardner D, Ulke AG, Torres Brizuela M, Kucienska B (2013) The environmental impact of the Puyehue–cordon Caulle 2011 volcanic eruption on Buenos Aires. Natural Hazards and Earth System Science 13:2319–2330CrossRefGoogle Scholar

56. Rose WI, Durant AJ (2011) Fate of volcanic ash: aggregation and fallout. Geology 39:895–896CrossRefGoogle Scholar

57. Satheesan K & Krishna Murthy B (2002) Turbulence parameters in the tropical troposphere and lower stratosphere. Journal of Geophysical Research: Atmospheres (1984–2012) 107:ACL 2–1-ACl 2–13Google Scholar

58. Saubin E, Tuffen H, Gurioli L, Owen J, Castro JM, Berlo K, McGowan E, Schipper CI, Wehbe K (2016) Conduit dynamics in transitional rhyolitic activity recorded by tuffisite vein textures from the 2008-2009 Chaitén eruption. Frontiers in Earth Science 4:59CrossRefGoogle Scholar

59. Schipper CI, Castro JM, Tuffen H, James MR, How P (2013) Shallow vent architecture during hybrid explosive–effusive activity at Cordón Caulle (Chile, 2011–12): evidence from direct observations and pyroclast textures. J Volcanol Geotherm Res 262:25–37CrossRefGoogle Scholar

60. Schwaiger HF, Denlinger RP, Mastin LG (2012) Ash3d: a finite-volume, conservative numerical model for ash transport and tephra deposition. Journal of Geophysical Research: Solid Earth 1978–2012:117Google Scholar

61. Scollo S, Coltelli M, Bonadonna C, Del Carlo P (2013) Tephra hazard assessment at Mt. Etna (Italy). Nat Hazards Earth Syst Sci 13:3221–3233CrossRefGoogle Scholar

62. Scollo S, Del Carlo P, Coltelli M (2007) Tephra fallout of 2001 Etna flank eruption: analysis of the deposit and plume dispersion. J Volcanol Geotherm Res 160:147–164CrossRefGoogle Scholar

63. Sieh K & Bursik M (1986) Most recent eruption of the Mono Craters, eastern central CaliforniaGoogle Scholar

64. Tuffen H, Dingwell DB, Pinkerton H (2003a) Repeated fracture and healing of silicic magma generate flow banding and earthquakes? Geology 31:1089–1092CrossRefGoogle Scholar

65. Tuffen H, James MR, Castro JM, Schipper CI (2013) Exceptional mobility of an advancing rhyolitic obsidian flow at Cordón Caulle volcano in Chile. Nat Commun 4Google Scholar

66. Watt SF, Pyle DM, Mather TA, Martin RS, Matthews NE (2009) Fallout and distribution of volcanic ash over Argentina following the may 2008 explosive eruption of Chaitén, Chile. Journal of Geophysical Research: Solid Earth 1978–2012:114Google Scholar

67. Wen C, Yu Y (1966) A generalized method for predicting the minimum fluidization velocity. AICHE J 12:610–612CrossRefGoogle Scholar

68. Wilson CJ, Hildreth W (1997) The bishop tuff: new insights from eruptive stratigraphy. J Geol 105:407–440CrossRefGoogle Scholar

69. Wilson L, Huang T (1979) The influence of shape on the atmospheric settling velocity of volcanic ash particles. Earth Planet Sci Lett 44:311–324CrossRefGoogle Scholar

70. Woods A (2013) Sustained explosive activity: volcanic eruption columns and Hawaiian fountains. Modeling Volcanic Processes: The Physics and Mathematics of Volcanism 153Google Scholar